Colloidal CdSe/CdS Dot-in-Plate Nanocrystals with 2D-Polarized Emission

Elsa Cassette, Benoît Mahler, Jean-Michel Guigner, Gilles Patriarche, Benoît Dubertret, and Thomas Pons

Supporting information

A. Calculation of the quantity of precursors injected for each layer:

To calculate the quantity of the shell precursors we have to introduce for each "monolayer", we first estimate the concentration of the CdSe core solution. We measured the absorption of the solution at 350 nm which is proportional to the volume of the particles and to their concentration.[1] The mean size of the CdSe NCs was determined by the position of the first absorption peak and the formula of Yu *et al.*.[2] A typical core synthesis gave 10 mL of CdSe NCs in hexane at ~80 μM. We calculated the volume of CdS for each monolayer (0.34 nm of thickness) and we calculated the corresponding quantity of Cd- and S- precursors we have to add. Experimentally, we found that the final spherical core/shell NCs were larger than predicted. We thus introduced a factor 1.5 to reduce the quantity of precursor introduced at each monolayer. For example, for initial cores of 1.62 nm (samples P), using 2 mL of solution of ~80 μM of CdSe NCs, the calculated volumes of Cd- and S- precursors at 0.1M were:

CdS ML	1°	2°	3°	4°	5°	6°	7°	8°
V 0.1M (mL)	0.23	0.35	0.48	0.63	0.80	0.99	1.21	1.44

We used the same 1.5 factor for both spherical and anisotropic shell growth. We noted that the final spherical NCs were still slightly larger than the predicted sizes.

B. Structural characterizations

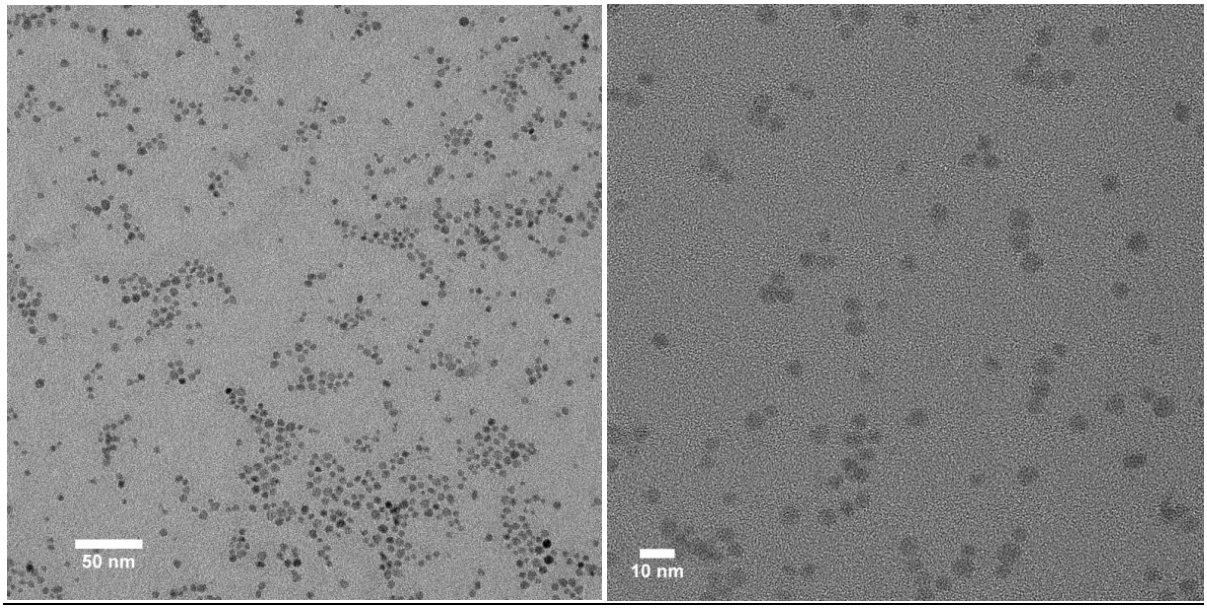

Figure S1: TEM pictures of CdSe/CdS dot-in-plate with 2 equivalent CdS monolayers on 1.62 nm cores (sample P2). Magnification: left 80k, right 200k.

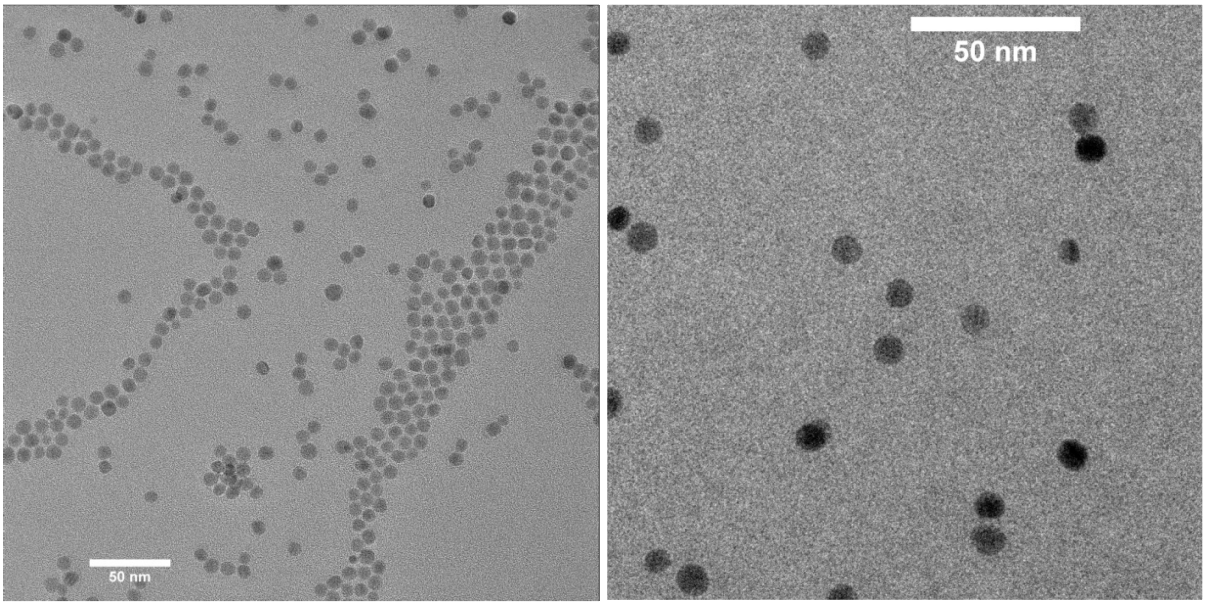

Figure S2: Spherical CdSe/CdS NCs with 6 CdS monolayers (sample S6) on 1.55 nm cores. Left panel: TEM picture at 120k magnification. Right: Cryo-TEM picture with NCs in all orientations, at 120k magnification.

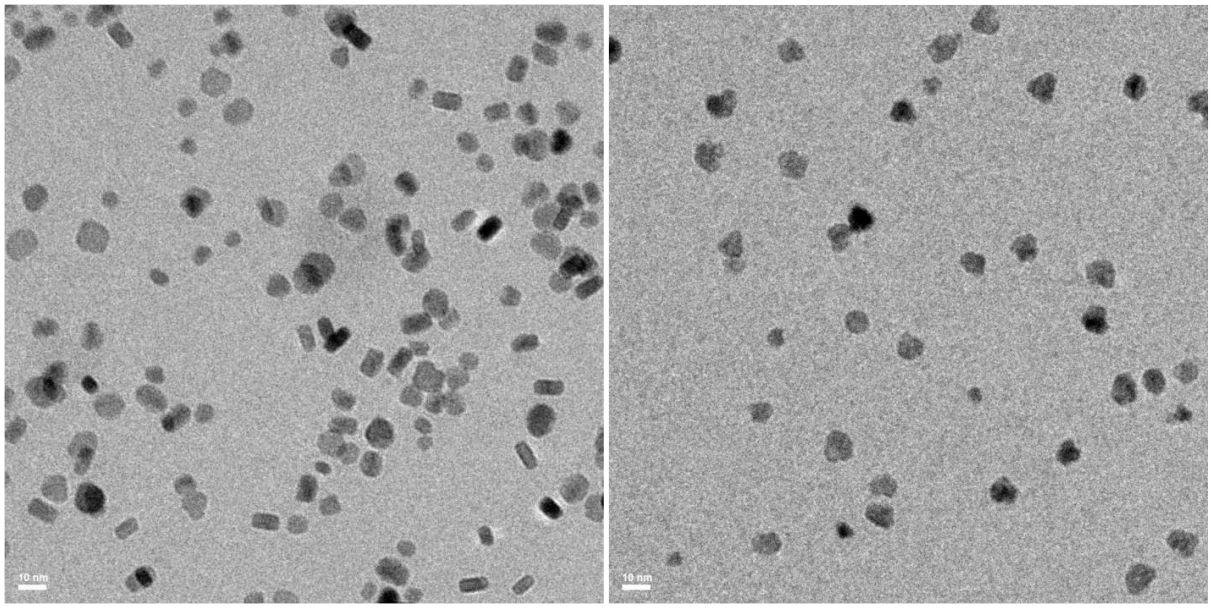

Figure S3: Left: Cryo-TEM (100k magnification) of CdSe/CdS dot-in-plate NCs with 6 CdS equivalent monolayers (cores: 1.63 nm). Right: Cryo-TEM (120k magnification) of CdSe/CdZnS NCs.

Size measurements:

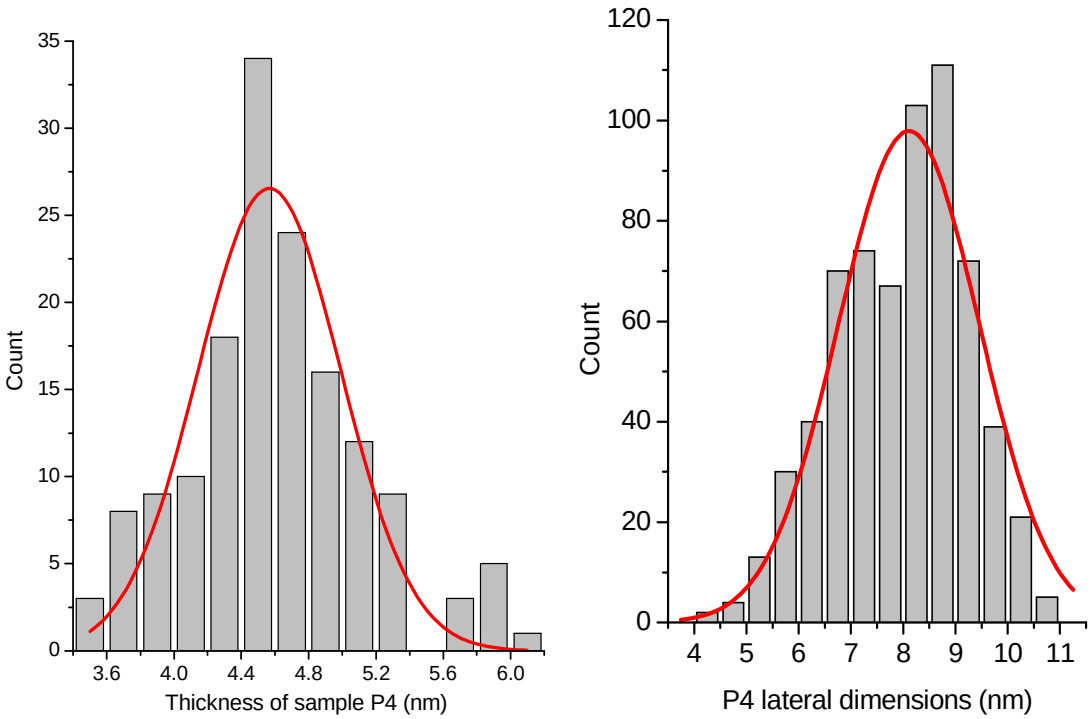

Figure S4: Histograms of sizes from TEM measurements of sample P4 (with 4 equivalent CdS monolayers on 1.62 nm cores).

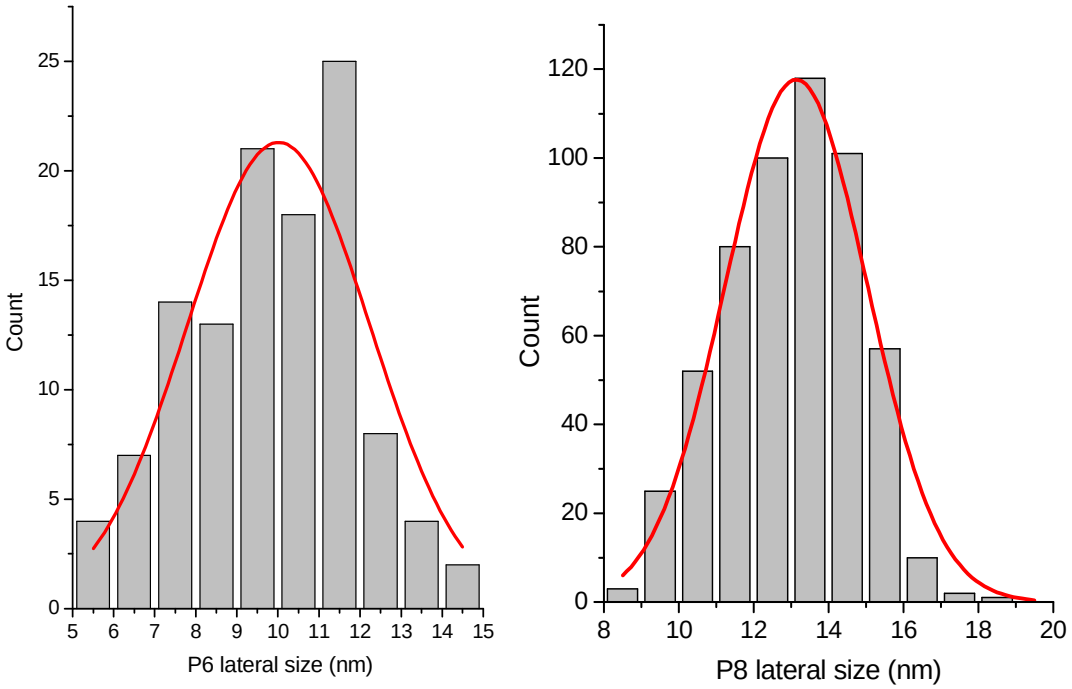

Figure S5: Histograms of lateral sizes from TEM measurements of samples P6 and P8 (with 6 and 8 equivalent CdS monolayers on 1.62 nm cores).

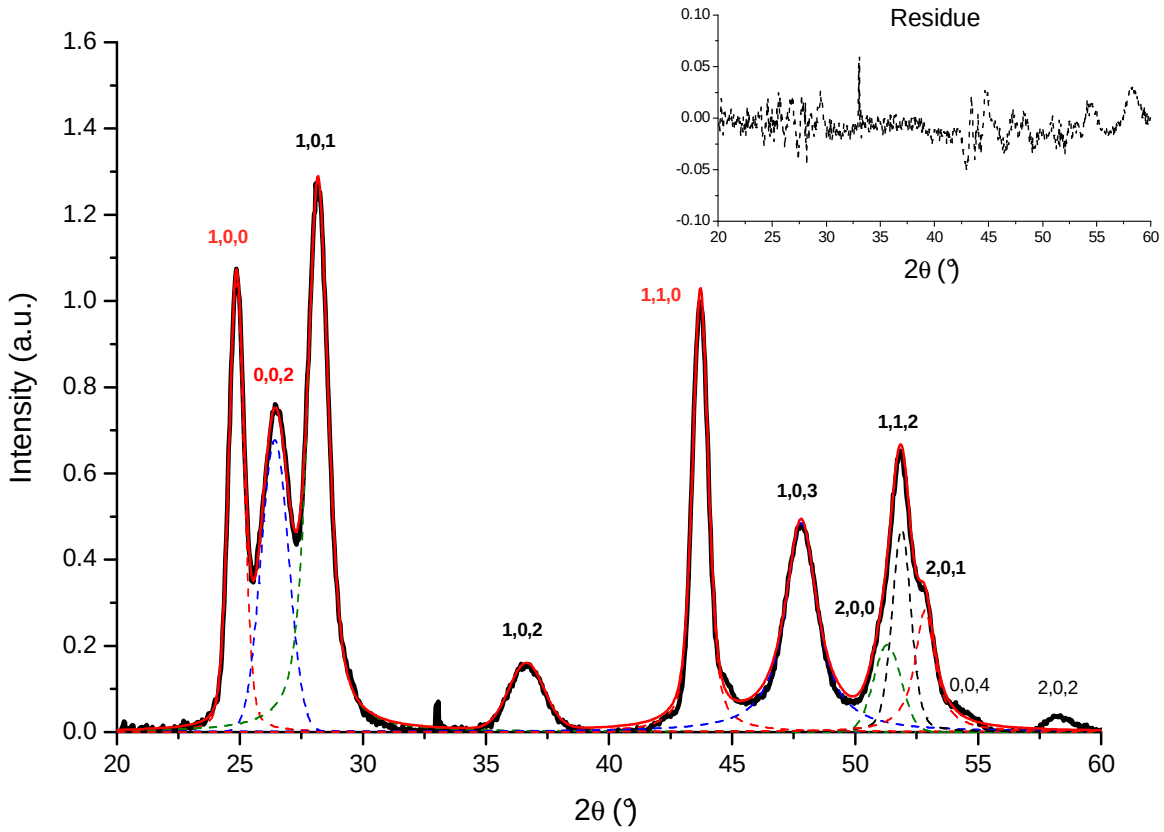

Figure S6: XRD profile of sample P8 (in black), with 8 CdS equivalent monolayers on 1.62 nm cores. Peak widths were extracted from pseudo-Voigt fit (in red) in order to estimate the thickness of the NCs. Inset: fit residue.

CdSe core localization in the flat CdS shell:

HAADF images were obtained on an aberration-corrected STEM (Jeol 2200FS) operating at 200 kV and equipped with an EDX spectrometer. The probe size was 0.1 nm (FWHM) and the current probe 50 pA. The half-angle of convergence of the probe was 30 mrad. The half-angle of detection for the dark field (DF) detector was set between 100 mrad (inner) and 170 mrad (outer). The EDX elemental mapping have been obtained with a current probe of about 240 pA (probe size 0.15 nm) using the K_α lines for the sulphur and the selenium and $L\alpha$ line for the cadmium.

We use a NC sample with a minimum of CdS grown along the c axis (around 1-2 monolayers), with approximatively 4 CdS equivalent monolayers on ~3.2 nm CdSe cores.

To avoid contamination under the electronic beam, a large excess of octylamine was first added in the NC solution (in hexane), then heated at ~65° for ~15 mn and washed by several cycles of precipitations/redispersions (with ethanol and isopropanol as polar solvents and chloroform or hexane for redispersion). Then, one drop of solution is deposited on a TEM grid and the sample was dried under vacuum for at least two days.

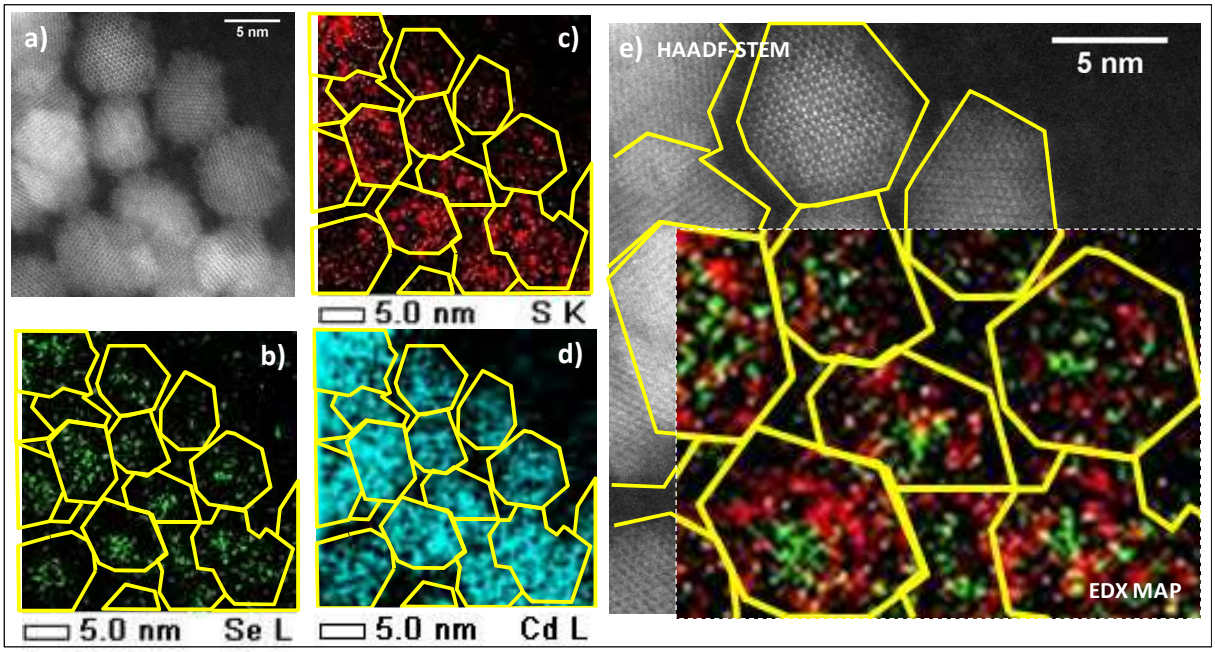

Figure S7: EDX-STEM analysis of dot-in-plate NCs: a) HAADF-STEM picture; b), c) and d) chemical mapping of Se (L line), S (K line) and Cd (L line) elements, respectively. The yellow lines represent the outline of the NCs, determined from image a). The inset in picture e) is the map of the superposition of Se (green) and S (red) elements.

Figure S7 shows that CdSe cores are localized near the center of the CdS shell in the (a, b) plane. Figure S7-b shows that the signal from the Se L line is more intense on areas near the center of the NC plane. In contrast, Figure S7-c shows that signal from the S K line is mostly distributed in the periphery of the dot-in-plate. Finally, the Cd map (figure S7-d) shows more uniform intensities over the whole NC. This is consistent with a CdSe/CdS core/shell structure with the CdSe core in the center of the dot-in-plate (a,b) plane.

To quantify more precisely the composition of the dot-in-plate NCs, we performed EDX measurements on small areas in the NCs, The results are shown in figure S8. For all NC centers, the proportion of Se is at least 10 % and, most of the time, is higher than those of the periphery. When averaged over all measured areas, the proportion of Se in the center areas is significantly higher than on the periphery of the NCs (17% vs. 6%). These measures confirm again that the CdSe cores are localized near the center of the dot-in-plate (a,b) plane.

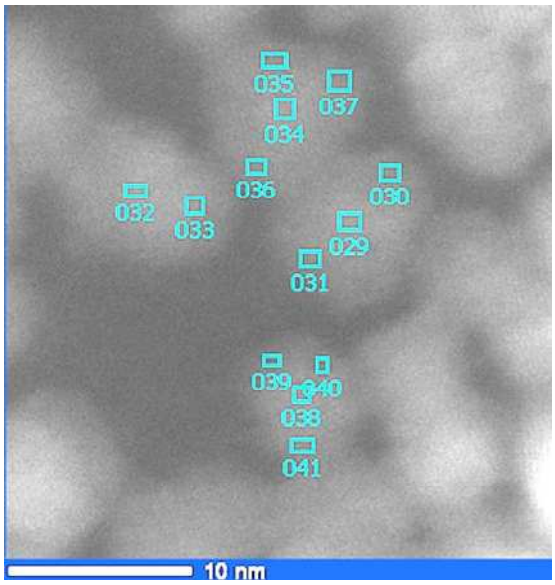

		S (atom%)	Se (atom%)	Cd (atom%)
QD1	**Center - 29**	**34.65**	**10.25**	**55.1**
	Periphery -30	24.77	7.42	67.81
	Periphery -31	25.69	13.54	60.77
QD2	**Center – 32**	**18.2**	**15.03**	**66.78**
	Periphery – 33	35.69	0	64.31
QD3	**Center - 34**	**18.89**	**19.87**	**61.23**
	Periphery - 35	20.71	17.25	62.05
	Periphery - 36	36.6	0	63.4
	Periphery - 37	25.74	0	74.26
QD4	**Center - 38**	**27.41**	**22.24**	**50.35**
	Periphery - 39	53.64	11.65	52.71
	Periphery - 40	35.77	0	64.23
	Periphery - 41	24.74	0.36	74.9
Average QD Center		**24.79**	**16.85**	**58.37**
Average QD Periphery		31.48	5.58	64.94

Figure S8: Left: CdSe/CdS dot-in-plate picture (dark field) with selected areas Right: corresponding S,Se and Cd atomic proportions.

Geometrical phase analysis:

We have used the Geometrical Phase Analysis (GPA) method to spatially map in detail the strain fields inside the core/shell quantum dots.[3-4] The GPA method has been applied from HRTEM images and atomic resolution HAADF-STEM images. All phase images have been calculated from two (1 -1 0 0) peaks of the FFT. The x axis is systematically aligned with a <1 1 -2 0> direction of the nanocrystal. The spatial resolution of the strain map, fixed by the mask diameter selected for the phase image calculation, is given at about 1.2nm. The comparison between strain maps obtained from HRTEM or HAADF-STEM images shows very similar results. However, a strain map established from an HAADF-STEM image generally appears less noisy.

Figure S9 shows two examples of deformation maps obtained by GPA for dot-in-plate nanocrystals. They show a clear deformation of the lattice near the center of the core/shell dot-in-plate structure, which we interpret as the signature of the CdSe core localization. The amplitude of the deformation is around 5-6 %, which is consistent with the expected values for the lattice mismatch between the CdSe cores and the CdS shell (3.8 % of lattice mismatch between unconstrained CdSe and CdS + 1.2 % due to anisotropic pressure of the shell on the core, as estimated from our model of strain, see below).

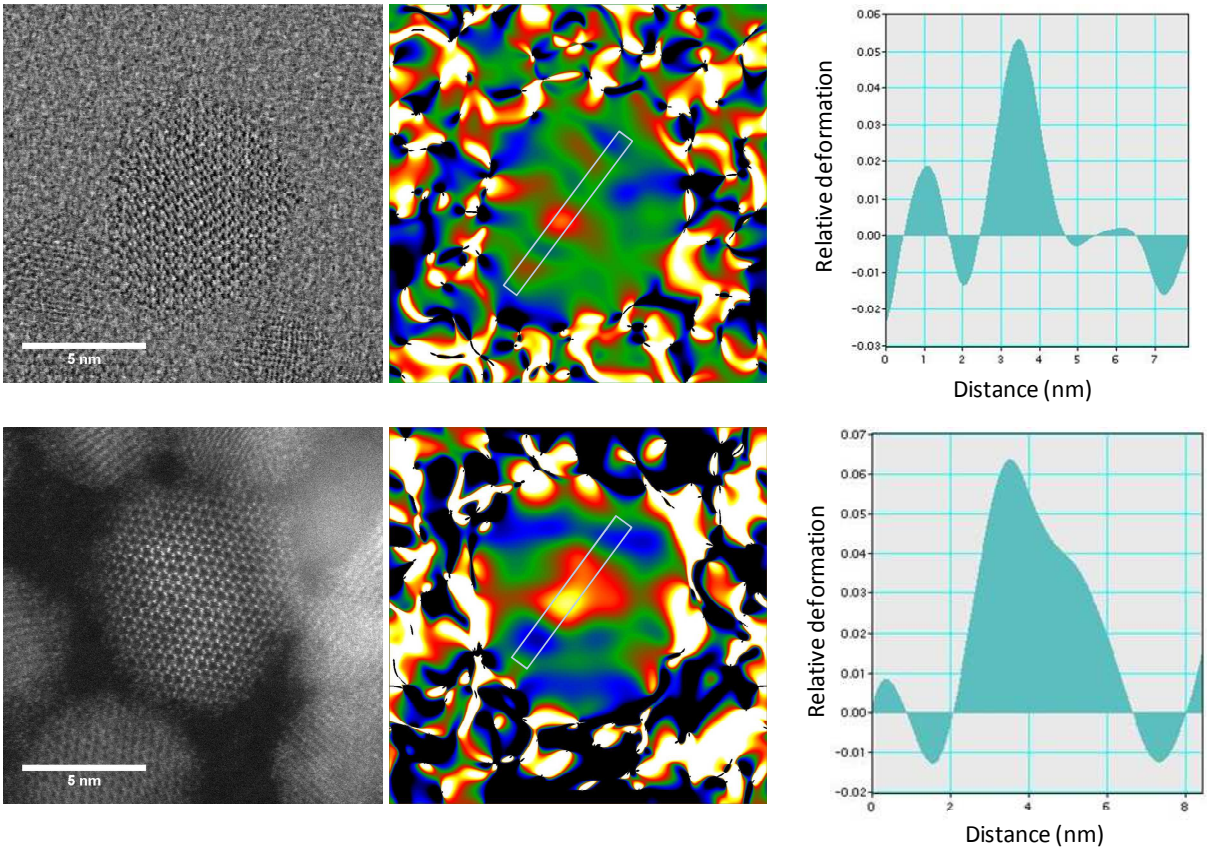

Figure S9: Two examples of GPA performed on dot-in-plate images. Left column: HAADF-STEM images; Middle column: deformation map obtained by GPA; Right column : line profile of the deformation.

C. Optical characterizations:

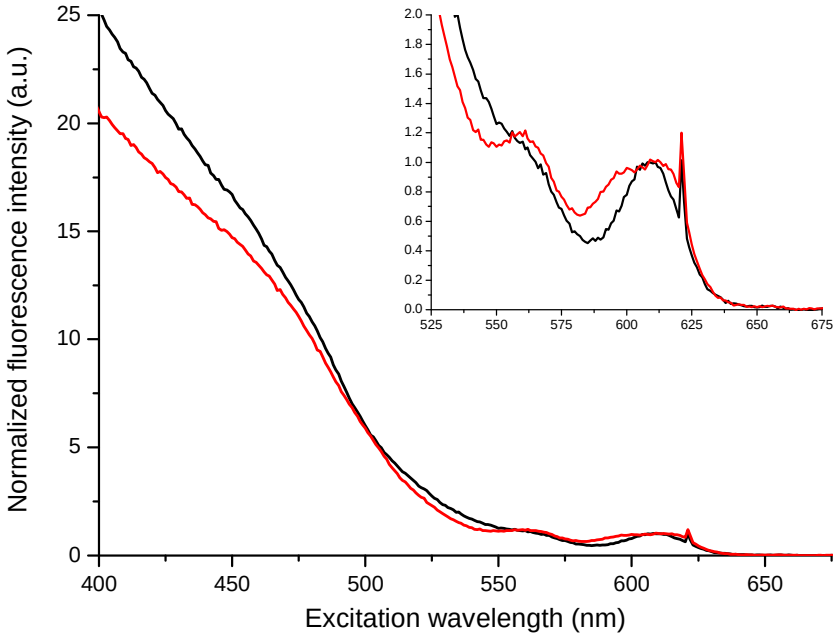

Figure S10: PLE spectra of spherical (dark line) and dot-in-plate (red line) CdSe/CdS NCs with 6 (equivalent) CdS monolayers on ~3 nm core. Inset: zoom.

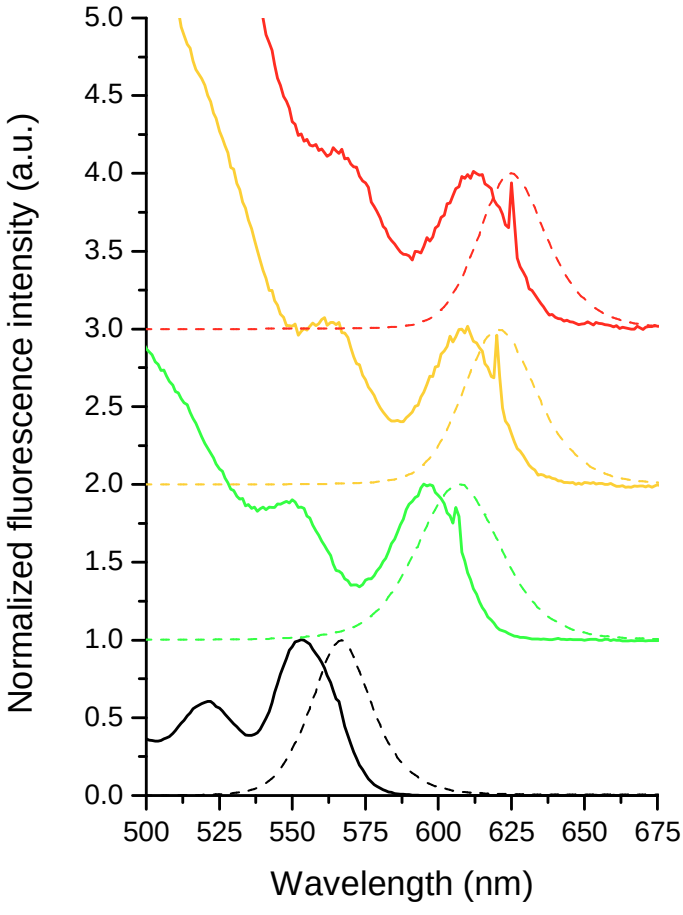

Figure S11: PL (dashed lines) and PLE (full lines) spectra of spherical CdSe cores (black) and spherical CdSe/CdS NCs with 2, 4 and 6 equivalent CdS monolayers on 1.56 nm cores (from green to red).

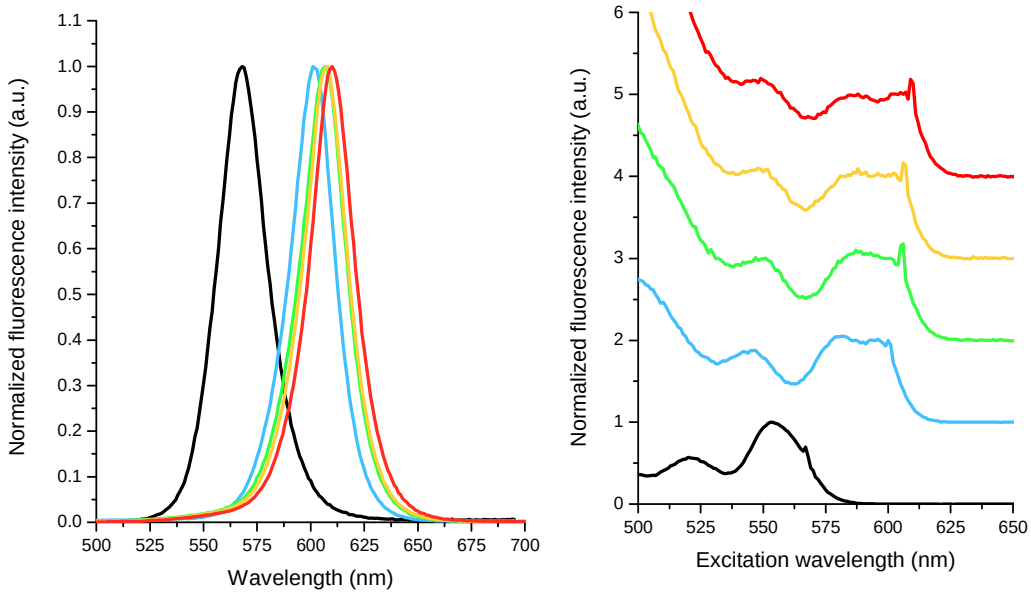

Figure S12: PL (left) and PLE (right) spectra of CdSe (black) and CdSe/CdZnS NCs during the CdZnS alloy growth on 1.59 nm cores (from blue to red).

Definition of heavy hole and light hole excitons:

Following ref. 5, the state energy and wave-function depend on two terms: Δ corresponds to the crystal asymmetry (structure, shape but also the pressure, see below) and η corresponds to a term due to the electron-hole exchange interaction. In our case, Δ is on the order of 60 meV (see below) compared to only a few meV due to electron delocalization in the CdS shell.[6] When Δ>>η, we can rewrite the energy of the different states:[5, 7]

$$E_{\pm 2} \approx E_{\pm 1^L} \approx -\frac{\Delta}{2}$$

$$E_{0^U} \approx E_{0^L} \approx E_{\pm 1^U} \approx +\frac{\Delta}{2}$$

and their corresponding wave-functions:

$$\Psi_{+2} = \Psi_{\uparrow,+3/2}$$

$$\Psi_{-2} = \Psi_{\downarrow,-3/2}$$

$$\Psi_{+1^L} \approx \Psi_{\downarrow,+3/2}$$

$$\Psi_{-1^L} \approx +i.\Psi_{\uparrow,-3/2}$$

The ± 2 and $\pm 1^L$ states depend thus only of the heavy hole band (Bloch functions $u_{+3/2}$ and $u_{-3/2}$) in the valence band. All these states close in energy form the heavy hole exciton (HX).

And:

$$\Psi_{+1^U} \approx -i.\Psi_{\uparrow,+1/2}$$

$$\Psi_{-1^U} \approx \Psi_{\downarrow,-1/2}$$

$$\Psi_{0^U} = \frac{1}{\sqrt{2}}.\left(-i.\Psi_{\uparrow,-1/2} + \Psi_{\downarrow,+1/2}\right)$$

$$\Psi_{0^L} = \frac{1}{\sqrt{2}}.\left(+i.\Psi_{\uparrow,-1/2} + \Psi_{\downarrow,+1/2}\right)$$

The states $\pm 1^U$, 0^U and 0^L therefore take into account only the light hole band in the valence band (Bloch functions $u_{+1/2}$ and $u_{-1/2}$). They form the light hole exciton (LX).

D. Model of strain in dot-in-plate nanocrystals

We assume for simplicity a cylindrical geometry around the c axis, and that the CdS shell grows only in the (a,b) plane, not along the c axis. Even though the core is spherical instead of cylindrical, this provides a good first approximation of the strains in the core and the shell materials. In addition, we assume isotropic elasticity properties for each material. The model of strain is based on the calculation of the displacements in hollow cylinders representing the core and the shell, respectively. According to reference [8], the radial and vertical displacements, u_r, u_z take the general form:

$$u_r = A\,r + B/r, \quad u_z = e\,z$$

We further assume that

(i) the pressure is continuous at the interface between the core and the shell, at $r = R_0$: $P(R_0) = P_0$,

(ii) the pressure at the NC surface, i.e. at the shell outer radius $r = R_s$ and on the upper and lower faces of the plate, is zero.

(iii) the growth of the shell on the core is epitaxial. This imposes $u_r^{core}(R_0) - u_r^{shell}(R_0) = \varepsilon R_0$, where $\varepsilon = (a_{CdSe} - a_{CdS})/a_{CdSe}$ is the lattice mismatch.

Following reference [8], and noting $\alpha = R_s/R_0$, conditions (i) and (ii) provide the following expressions:

$$A_{core} = -\frac{P_0}{2(\lambda_c+\mu_c)}\left(1 + \frac{{\lambda_c}^2}{\mu_c(3\lambda_c+2\mu_c)}\right),\ B_{core} = 0,\ e_{core} = \frac{\lambda_c P_0}{\mu_c(3\lambda_c+2\mu_c)},$$

$$A_{shell} = \frac{P_0}{2(\lambda_s+\mu_s)(\alpha^2-1)}\left(1 + \frac{{\lambda_s}^2}{\mu_s(3\lambda_s+2\mu_s)}\right),\ B_{shell} = \frac{P_0 {R_s}^2}{2\mu_s(\alpha^2-1)},\ e_{shell} = \frac{-\lambda_s P_0}{\mu_s(3\lambda_s+2\mu_s)(\alpha^2-1)}$$

where $\lambda_{c,s}$ and $\mu_{c,s}$ are Lamé's parameters of the core and the shell, respectively. Then using the above relations together with condition (iii) we obtain the value of P_0 as a function of

Lamé's parameters. From this we can calculate the diagonal components of the stress tensor in the CdSe core:

$$\varepsilon_{rr} = \frac{\partial u_r}{\partial r} = A_{core}\ , \quad \varepsilon_{zz} = \frac{\partial u_z}{\partial z} = e_{core}.$$

Finally, neglecting the electron-hole exchange interaction, the splitting between the "heavy hole" and the "light hole" exciton (HX and LX, respectively) levels is expressed as: [5, 9]

$$E_{LX} - E_{HX} = -(E_{LH} - E_{HH}) = \Delta_{\text{int}} + \Delta_{\varepsilon}$$

where Δ_{int} (= 25 meV) is due to the crystal field splitting, and Δ_{ε} is the splitting due to strain:[5, 9]

$$\Delta_{\varepsilon} = -\frac{2}{3}(D_3.\varepsilon_{zz} + D_4.\varepsilon_{rr}).$$

Here we assume pure HH or LH contribution in HX and LX transitions, respectively (see above).

For simplicity, we assume homogeneous elastic properties for the core and the shell and we take λ_c= 55 GPa, μ_c=19.3 GPa,[10] D_3 = -2.94 eV, D_4 = 1.47 eV and a lattice mismatch of 3.8 % between CdSe and CdS. The obtained heavy hole-light hole splitting is represented in figure S13 as a function of the ratio between the core and the shell outer radii (no adjustable parameters).

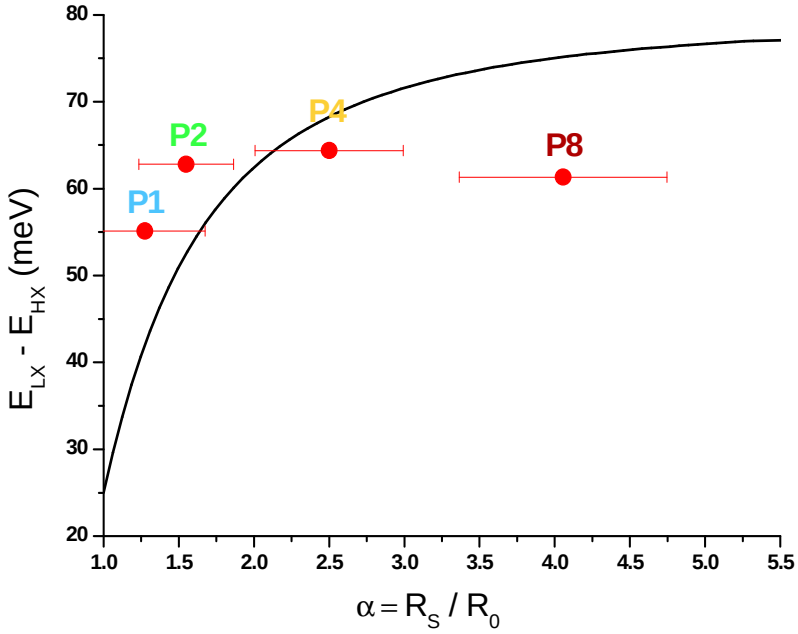

Figure S13: Prediction of the heavy hole-light hole exciton splitting as a function of the ratio between the core and the shell radii (black line, no adjustable parameters). Values for samples P1, P2, P4 and P8 are indicated with red dots (with 1, 2, 4 and 8 equivalent CdS monolayers, respectively).

The model correctly predicts the evolution of the splitting as a function of shell thickness: the experimental data show a gradual increase, with a rapid saturation after a few monolayers. The maximum splitting value is about 65 meV, consistent with the theoretical value of ~ 77 meV. Discrepancies between the model and the data could come from different reasons:

1) The geometry of the core is spherical instead of cylindrical. This difference could prove important especially for the thin shell samples.

2) The shell thicknesses were difficult to evaluate for samples P1 and P2 and present large relative errors.

3) Sample P8 shows a splitting that is less than sample P4. This might be due to growth of some CdS in the c-axis direction, as shown in the size measurements (figure 5 in the manuscript). This would reduce the anisotropy of the pressure induced by shell in the core, and would lead to a decreased heavy hole-light hole splitting.

4) A possible alloying at the interface CdSe/CdS, most probably for larger sample may slightly reduce the pressure induced by the shell.

E. Excitation anisotropy:

Principle:

Transition dipoles (of absorption and emission) have well defined orientations with respect to crystal axes (*i.e.* parallel or perpendicular to crystal c axis). Anisotropy measurements provide information about the orientation between the absorption and the emission dipoles. Briefly, NCs are solubilized in a viscous solution so that they are randomly oriented and their rotational diffusion is slower than their fluorescence lifetime. This solution is excited with vertically polarized light, leading to selective excitation of the population of NCs with an absorption dipole parallel to the vertical. We then compare the fluorescence intensities detected using a vertically and a horizontally polarized analyzer in the detection path (see schematic in figure S14). Roughly, when the vertically polarized signal is higher than the horizontally polarized one, this indicates that the emission dipole is parallel to the absorption dipole. In opposite, when the horizontally polarized signal is higher, this indicates that the emission dipole is perpendicular to the absorption dipole. Quantitative analysis of the anisotropy measured for different excitation wavelengths allows determining the angle between the different transition dipoles involved, and if they are oriented in one dimension or degenerate in a plane. We refer the reader to ref. 9 for additional details about anisotropy measurements.

Experimental details:

Excitation anisotropy was performed on a sample for which the splitting between the heavy and light hole bands is clearly visible (sample P4, light orange curves in figure 6).We used a dilute solution of these dot-in-plate NCs in polybutadiene. We verified using time-resolved anisotropy measurements that this solution was viscous enough to neglect rotation of the particles between their excitation and emission.
The measurements were made in an L configuration with the excitation polarized in vertical (V) position parallel to the lab z axis; and an emission polarized first vertically (V), along z; then horizontally (H), along the lab y axis (figure S14). The measured intensities, I_{VV} and I_{VH}, need to be corrected from the anisotropy introduced by the instrumentation detection path, to obtain the intrinsic parallel and perpendicular intensities ($I_{\parallel}$ and $I_{\perp}$). We used the following relation: [11]

$$\frac{I_{\parallel}}{I_{\perp}} = \frac{1}{G} . \frac{I_{VV}}{I_{VH}}$$

where G can be measured for each emission wavelength, with excitation polarized horizontally (i.e. along the x axis): $G=I_{HV}/I_{HH}$.[11]

The anisotropy factor is written using equation SE1:[11]

$$R = \frac{I_{\parallel} - I_{\perp}}{I_{\parallel} + 2.I_{\perp}} = \frac{I_{VV} - G.I_{VH}}{I_{VV} + 2.G.I_{VH}} \qquad \text{(SE1)}$$

PL spectra were recorded for each excitation wavelengths to probe the different excitation transitions. The intensities I_{VV} and $G.(I_{VH})$ were the integrated intensities from the central portion of the corresponding PL spectrum (~80 % of the signal), eliminating the peak tails. Finally, R was plotted *versus* the excitation wavelength (figure 8, black line).

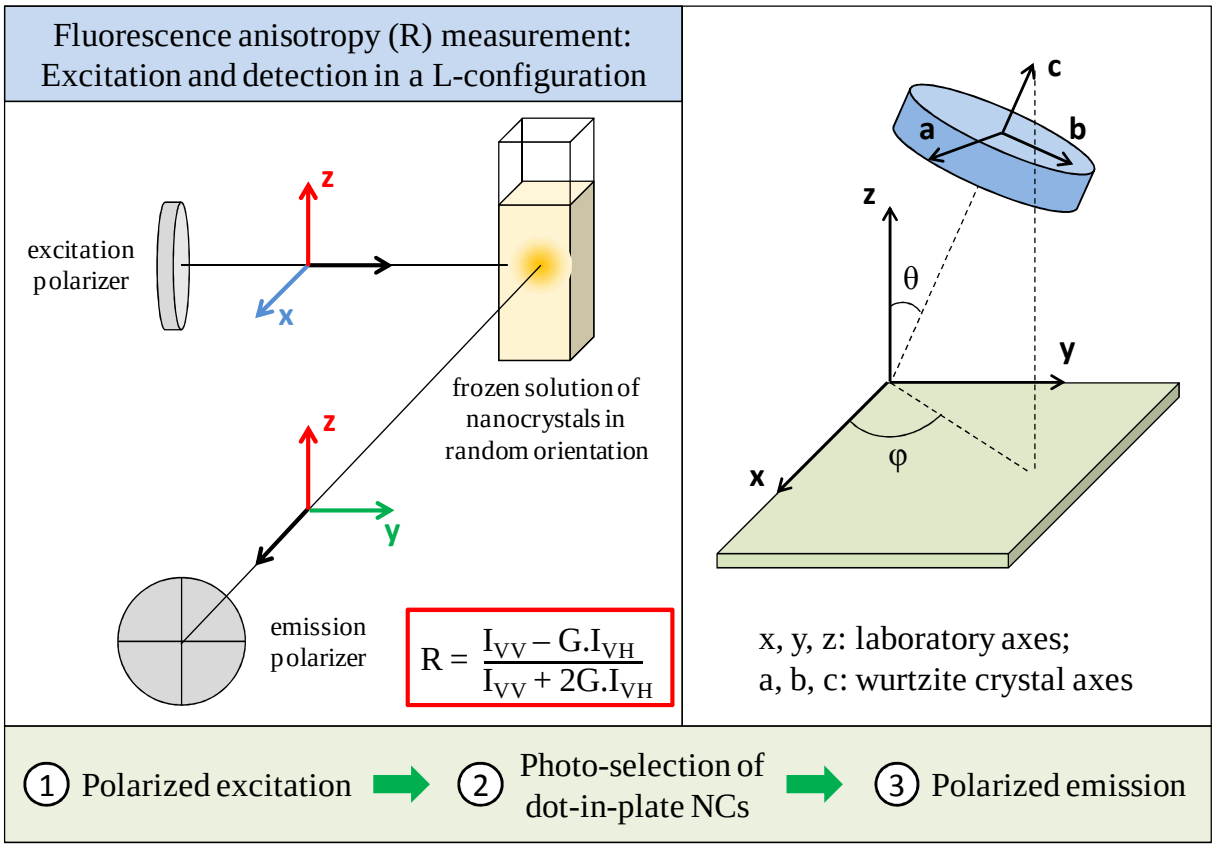

Figure S14: (left panel) Schematic diagram of anisotropy measurement setup and (right panel) projection of the crystal axes (a, b, c) on the laboratory references (x, y, z).

Theoretical predictions:

Using spherical coordinates, let θ be the angle between the laboratory z axis and the crystal c axis and φ the angle between the lab x axis and the projection of the crystal c axis in the (x,y) plane (figure S14, left). We have:

- The excitation probability of particles with excitation dipole orientation in the plane perpendicular to c, i.e. in the (a,b) plane, is proportional to $\sin^2(\theta)$. In the case of an excitation dipole parallel to c, the absorption is proportional to $\cos^2(\theta)$;
- For a 2D emission dipole in the (a,b) plane, the fluorescence emission polarized along the z axis (V) is proportional to $\sin^2(\theta)$; the fluorescence emission polarized along the y axis (H) is proportional to $[1-\sin^2(\theta).\sin^2(\varphi)]$;
- For a 1D emission dipole along the c axis, the fluorescence emission polarized along the z axis (V) is proportional to $\cos^2(\theta)$; the fluorescence emission polarized along the y axis (H) is proportional to $\sin^2(\theta).\sin^2(\varphi)$.

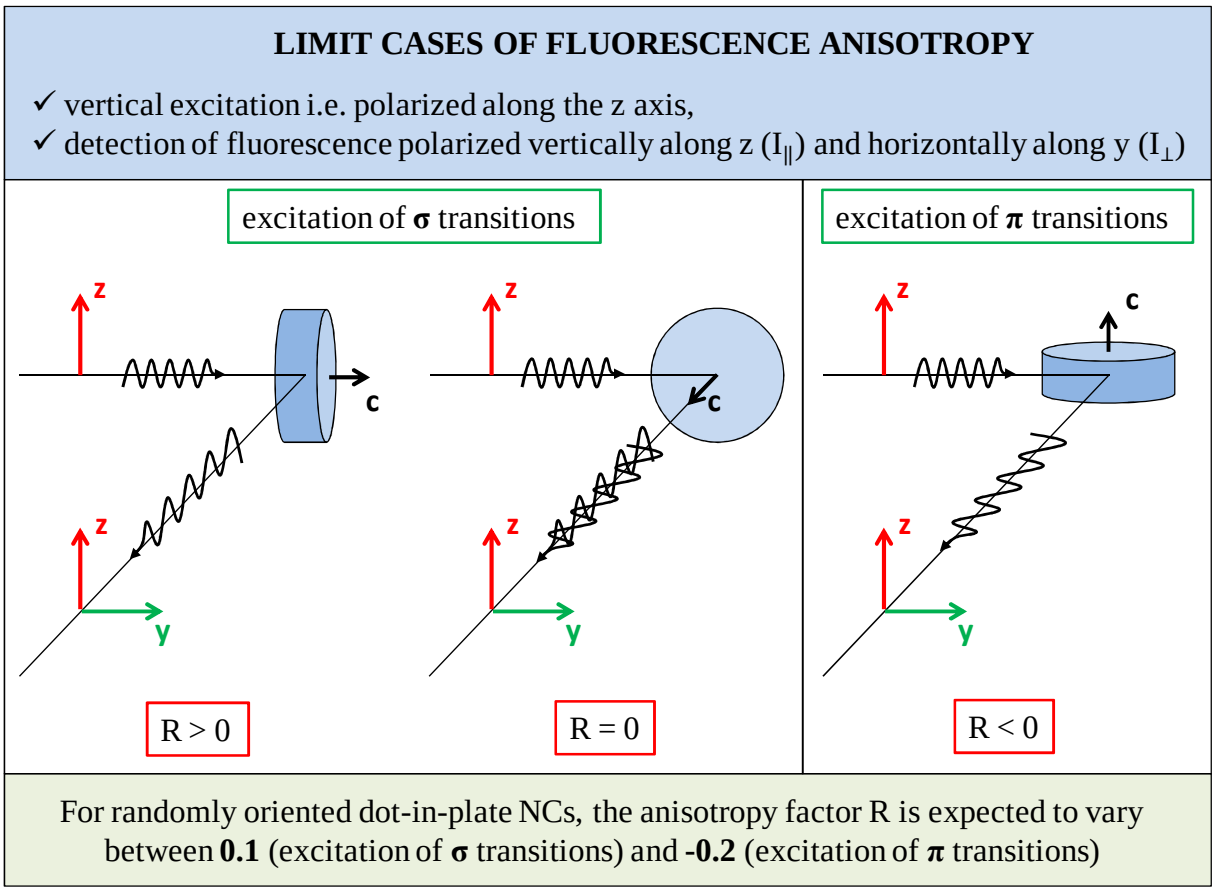

Figure S15: Schematic of anisotropy in the limit cases of oriented particles with the corresponding sign of the anisotropy factor R. The theoretical factor for randomly oriented particles is included in [-0.2; +0.1] (see the calculation below).

The intensity emitted with a polarization along z ($I_{\parallel}$) is proportional to:

$$I_{\parallel} \propto \int_0^{2\pi} \int_0^{\pi} [p_{\perp}.f_{\perp}.\sin^2(\theta) + p_{\parallel}.f_{\parallel}.\cos^2(\theta)].[f_{\perp}.p_1.t_1.\sin^2(\theta) + f_{\parallel}.p_0.t_0.\cos^2(\theta)].\sin(\theta).d\theta.d\varphi$$

And the intensity emitted with a polarization along y ($I_{\perp}$) is proportional to:

$$I_{\perp} \propto \int_0^{2\pi} \int_0^{\pi} [p_{\perp}.f_{\perp}.\sin^2(\theta) + p_{\parallel}.f_{\parallel}.\cos^2(\theta)].[f_{\perp}.p_1.t_1.(1-\sin^2(\theta).\sin^2(\varphi)) + f_{\parallel}.p_0.t_0.\sin^2(\theta).\sin^2(\varphi)].\sin(\theta).d\theta.d\varphi$$

With:

- $p_{\perp}$, the probability to excite a transition in the (a,b) plane which is excitation wavelength dependent;
- $p_{\parallel}$, the probability to excite a transition polarized along the c axis (excitation wavelength dependent);
- $f_{\perp}$, the dielectric factor for an excitation polarized in the (a,b) plane;
- $f_{\parallel}$, the dielectric factor for an excitation polarized along the c axis;
- p_1, the sum of oscillator strengths of the transition from the 1^U and 1^L states to the ground state;
- p_0, the oscillator strength of the transition from the 0^U state to the ground state;
- t_1, the population of the 1^U and 1^L states at thermal equilibrium; and

- t_0, the population of the 0^U state at thermal equilibrium.

In these formulas, $f_\perp$ is the exaltation square factor for anisotropic shape and $f_\parallel$ is the reduction square factor of the incoming or outgoing electric field due to the anisotropic shape and to the difference in dielectric constants between the semiconductor and the surrounding medium (see below). The factors t_1 and t_0 are dependent on the temperature of the medium and on the difference of energy between the 1^L, 1^U and 0^U states.

Integrating over all orientation angles yields:

$$I_\parallel \alpha \frac{4.\pi}{15}.[p_1.t_1.(8.p_\perp.f_\perp^2 + 2.p_\parallel.f_\parallel.f_\perp) + p_0.t_0(2.p_\perp.f_\perp.f_\parallel + 3.p_\parallel.f_\parallel^2)]$$

$$I_\perp \alpha \frac{4.\pi}{15}.[p_1.t_1.(6.p_\perp.f_\perp^2 + 4.p_\parallel.f_\parallel.f_\perp) + p_0.t_0(4.p_\perp.f_\perp.f_\parallel + p_\parallel.f_\parallel^2)]$$

and we can express the anisotropy factor as follows :

$$R = \frac{I_\parallel - I_\perp}{I_\parallel + 2.I_\perp} = \frac{2}{5}.\frac{[p_1.t_1.(p_\perp.f_\perp^2 - p_\parallel.f_\parallel.f_\perp) + p_0.t_0.(-p_\perp.f_\perp.f_\parallel + p_\parallel.f_\parallel^2)]}{[p_1.t_1.(4.p_\perp.f_\perp^2 + 2p_\parallel.f_\parallel.f_\perp) + p_0.t_0.(2.p_\perp.f_\perp.f_\parallel + p_\parallel.f_\parallel^2)]} \quad \text{(SE2)}$$

For isotropic particles, without any shape effect ($f_\parallel = f_\perp$), and neglecting the emission and absorption with polarization parallel to the crystal c axis (p_0, $p_\parallel = 0$), the maximum of anisotropy is obtained when the excitation and the emission have the same orientation, in the (a,b) plane of the crystals ($p_\perp = 1$, $t_1 = 1$, $p_1 = 1$):

$$R_{max} = 0.1;$$

Similarly, the minimum of anisotropy is obtained when the absorption dipole is along the c axis ($p_\parallel = 1$ and $p_\perp = 0$), whereas the emission dipole orientation is in the (a,b) plane ($t_1 = 1$, $p_1 = 1$):

$$R_{min} = -0.2;$$

At high energy, where there is no specific orientation of the absorption dipole, the anisotropy factor is zero for isotropic particles (no dielectric shape effect). To check that, we measured the excitation wavelength- dependent anisotropy factor of spherical CdSe/CdS NCs (sample S6). The resulting curve was represented in figure S16.

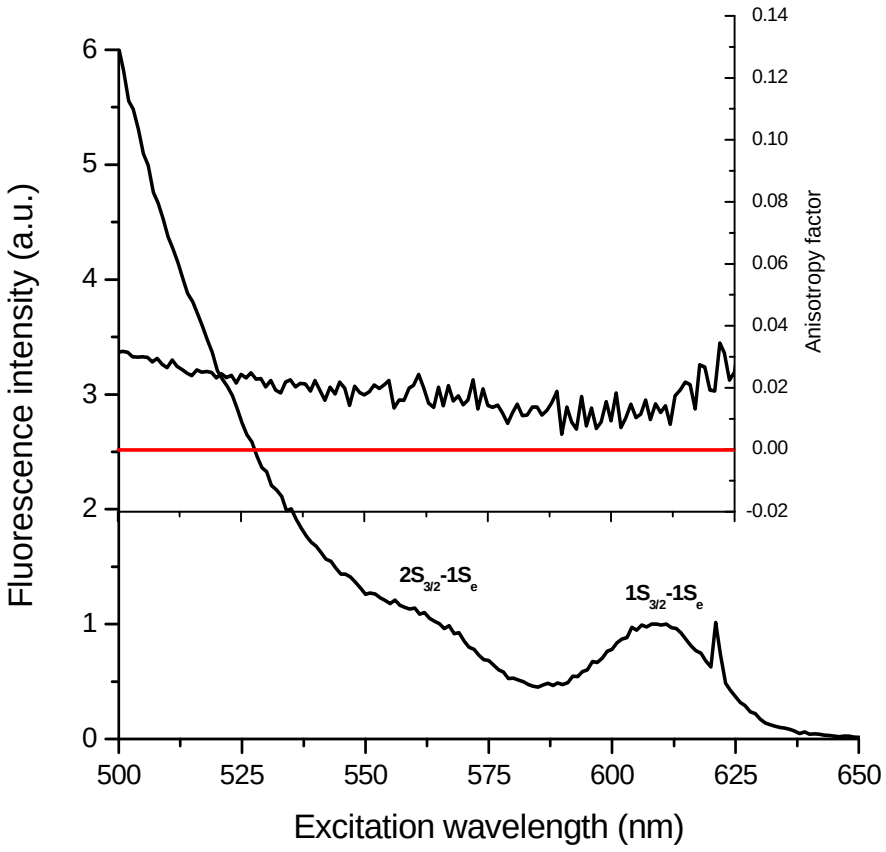

Figure S16: Upper black line: anisotropy factor of spherical CdSe/CdS NCs (sample S6). The theoretical curve is shown in red (R=0). The lower graphic represents the photoluminescence intensity at the corresponding excitation wavelengths (PLE spectrum).

The anisotropy curve in figure S13 is quasi constant and close to zero and thus shows no photo-selection of nanocrystals, consistently with the isotropic dipole orientation in excitation. Discrepancies between the model and the data (<0.02) could come from an inaccurate estimation of the instrumentation factor G.

Dielectric and shape effect:

The amplitude of an electric field at the interface of two dielectric media can be modified if one of the dielectric has a non isotropic shape.[12] We calculate this effect on the electric field penetrating a CdS "plate":

The plate is approximated by an oblate ellipsoid with the semi-axes a=b>c. The dependence of the aspect ratio on the dielectric effect is expressed as a function of the eccentricity (e) and is defined by:

$$e = \sqrt{\left(\frac{a}{c}\right)^2 - 1}$$

The ratio of the internal electric field parallel to that perpendicular to the crystal c axis ($E_{\parallel(int)}$ and $E_{\perp(int)}$ respectively) is:[12]

$$\frac{E_{\perp(int)}}{E_{\parallel(int)}} = \frac{E_{\perp(ext)}}{E_{\parallel(ext)}} \cdot \frac{\varepsilon^m + \left(\varepsilon^{int} - \varepsilon^m\right).n_{\parallel}}{\varepsilon^m + (\varepsilon^{int} - \varepsilon^m).n_{\perp}}$$

Where

- $n_{\parallel} = \frac{1+e^2}{e^3}.[\mathrm{e} - \mathrm{arctg(e)}]$; and $n_{\perp} = \frac{1}{2}.(1 - n_{\parallel})$ are the depolarization coefficients, parallel and perpendicular to the crystal c axis, respectively; $n_{\parallel} = n_{\perp}$ for isotropic particles.

- ε^{int} and ε^m are the dielectric constants of the plate (=5.5 for CdS), and of the medium (≈ 2.2 for the polybutadiene), respectively;

- $E_{\parallel(ext)}$ and $E_{\perp(ext)}$ are the external electric fields components polarized along the c axis and perpendicular to it, respectively.

In addition to the electronic probabilities of absorption, particles that have their c axis aligned with the excitation polarization will absorb even less due to this shape effect. On the contrary, excitation of particles which have their (a,b) plane parallel to the excitation field will be exalted. This leads to a higher photo-selection of NCs. In particular, this leads to a non-zero anisotropy at low wavelengths excitation, even though electronic transitions are intrinsically isotropic in this region.

Theoretical predictions of the anisotropy for sample P4:

The dimensions of the NCs used for the measurement were: (8.1 ± 1.6) nm for the lateral sizes and (4.57 ± 0.5) nm for the thickness. So the resulting eccentricity was ~1.46. The ratio of the exaltation and reduction factor of the electric field intensity penetrating the crystal for polarizations parallel to the c axis and perpendicular due to the dielectric and shape effect is then:

$$\frac{f_{\parallel}}{f_{\perp}} \approx 0.63,$$

This ratio was assumed constant for all excitation wavelengths.

Since the energy level splitting due to the crystal asymmetry, Δ, is much larger than the splitting due to the electron-hole exchange interaction, η, we assumed that the oscillator

strengths (p) of transitions between the ground state and the 0^U, $\pm1^U$ and $\pm1^L$ states follow the relations:[5]

$$p(0^U) + p(1^U) = p(1^L) \qquad \text{(SE3)}$$
$$p(0^U) = 2.p(1^U) \qquad \text{(SE4)}$$

We then fitted the PLE spectrum of the sample by Gaussians, setting the areas to follow relations expressed in equations SE3 and SE4, and neglecting the difference energy between the states 0^U and 1^U:

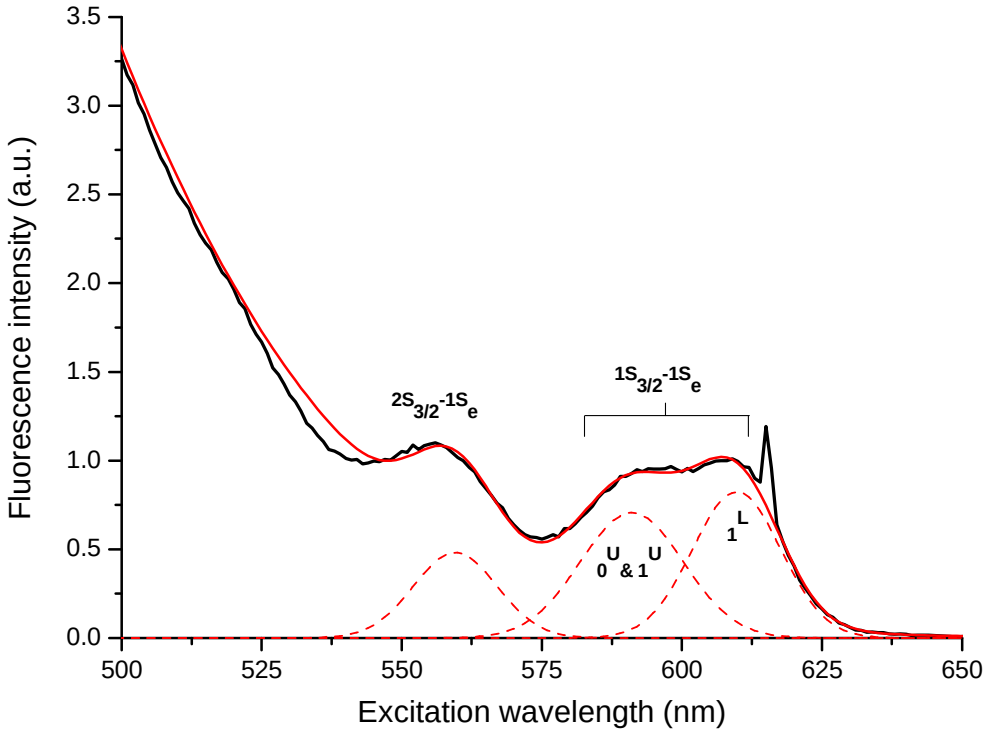

Figure S17: PLE spectrum of CdSe/CdS dot-in-plate NCs with 4 equivalent CdS monolayers on 1.62 nm cores (black curve). The sharp peak in the bandedge corresponds to scattering signal at the peak emission wavelength. The transitions of interest are presented (dashed lines in red) and are attributed to transitions from the ground state to $2S_{3/2}$-$1S_e$, 0^U with 1^U and 1^L states, from higher to lower energies.

For each excitation wavelength, we calculated the ratio of the probability to have an excitation parallel to the crystal c axis on those perpendicular ($\frac{p_\parallel}{p_\perp}$), using the values in table ST1, corresponding to the different transitions, and using the weight of each transitions at the excitation wavelength.

Transitions	$2S_{3/2}$-$1S_e$	$0^U + 1^U$	1^L
$p_\parallel$	1/3	2/3	0
$p_\perp$	2/3	1/3	1

Table ST1: Probabilities of excitation along the c axis ($p_\parallel$) and perpendicularly ($p_\perp$) for the different transitions. For $2S_{3/2}$-$1S_e$, the probability of transition is isotropic along a, b and c axis; The 0^U transition has an oscillator strength twice has much as the 1^U ones; and the transition dipoles of the 1L states are completely 2D, perpendicularly to the c axis.[5]

To estimate the part of the emission polarized along the c axis and the part polarized perpendicularly, we used the ratio of the oscillator strengths of 0^U on 1^L+1^U transitions

($\frac{p_0}{p_1}$)=0.5 (see equations SE3 and SE4) and their populations. The ratio $\frac{t_0}{t_1}$, at room temperature (kT ~ 25 meV), was estimated by the difference energy between the two lower transitions in the sample P4, following the Maxwell-Boltzmann statistics:

$$E_{0^U} - E_{1^L} \approx 64\ meV\ \approx E_{1^U} - E_{1^L}$$

And,

$$\frac{t_0}{t_1} = \frac{\exp\left(-\frac{E_{0^U} - E_{1^L}}{k.T}\right)}{2.\left[1 + \exp\left(-\frac{E_{1^U} - E_{1^L}}{k.T}\right)\right]} \approx 0.035$$

The factor 2 for 1^L and 1^U states comes from their multiplicities.

Finally, we calculate the anisotropy factor for each excitation wavelength, according to the equation SE2. These theoretical results are shown in figure 8, in red.

Theoretical calculation of the emission polarization ratio:

For the P4 sample with a splitting of 64 meV, taking into account the intrinsic oscillator strengths and the dielectric/shape effect, the ratio between 2D polarized emission and total emission is:

$$p_{em,2D} \approx \frac{f_{\perp}.t(1^L).p(1^L) + f_{\perp}.t(1^U).p(1^U)}{f_{\perp}.t(1^L).p(1^L) + f_{\perp}.t(1^U).p(1^U) + f_{\parallel}.t(0^U).p(0^U)}$$

$$\approx \frac{2.[\frac{1}{2} + \frac{1}{6}.\exp\left(-\frac{64}{25}\right)]}{2.\left[\frac{1}{2} + \frac{1}{6}.\exp\left(-\frac{64}{25}\right)\right] + 0.63.\frac{1}{3}.\exp\left(-\frac{64}{25}\right)} \approx 98.4\ \%$$

by using the relations SE3 and SE4 and the ratio $f_{\parallel}/f_{\perp}$=0.63 for sample P4.

Without taking into account the dielectric/shape effect, the proportion of 2D polarized emission would be 97.5 % ($f_{\perp}/f_{\parallel}$=1). The electronic splitting between HX and LX excitons is thus the most important cause of the 2D nature of the emission polarization.

F. Single nanocrystal polarization measurement

Dot-in-plates (sample P4) were deposited on a glass coverslip using spin-coating in a toluene/polymethylmethacrylate solution, so that we expect a random orientation in all three dimensions (the film thickness was about 200 nm – 1 µm). Fluorescence from isolated dot-in-plate NCs was collected using an inverted microscope (IX-71, Olympus) and a high numerical aperture objective (100x, NA 1.4), using an unpolarized excitation at 450 ± 25 nm. The two perpendicular polarization components (I_x and I_y) of their fluorescence were separated using a polarizing beamsplitter and simultaneously recorded on a CCD camera (see schematics in figure S18).

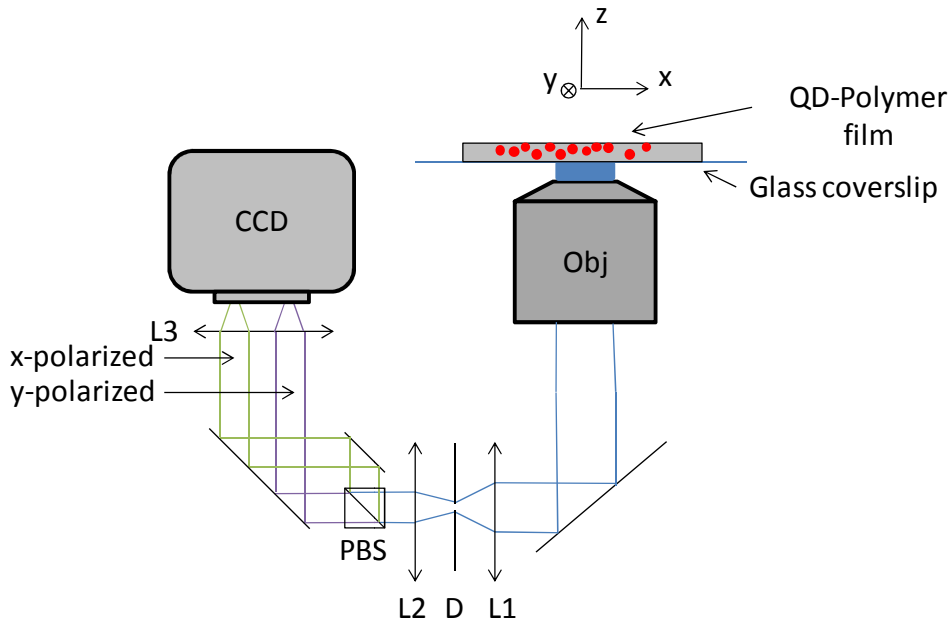

S18: Schematics of the single QD polarization ratio measurement, with microscope objective, lenses L1, L2, L3, diaphragm D and polarizing beam splitter PBS.

Fluorescence intensities were corrected from the background from neighboring pixels. Two typical traces corresponding to different NC orientations are presented in figure S19. The fluorescence intermittency (blinking) is perfectly correlated, which is consistent with detection of the same single NC in both channels. We then computed for more than 300 different single NCs the polarization ratio $r = I_x / (I_x + I_y)$. The obtained histogram is represented in figure S19.

Polarization ratio for 3D, 2D, and 1D emitters are given below as a function of their orientation with respect to the z optical axis of the microscope and the x and y axis of the sample plane:

1D emitters: 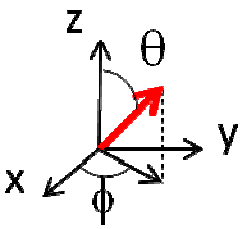 $r = \cos^2(\Phi)$

2D emitters: 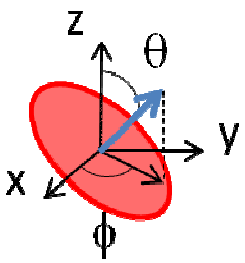 $r = (\cos^2(\theta)+\sin^2(\theta)\sin^2(\Phi)) / (1+\cos^2(\theta))$

3D emitters: –

From these expressions we calculate the theoretical predictions for a histogram of polarization ratios for 1D, 2D and 3D emitters, as shown in figure S19. The polarization ratio histogram from 1D emitters would present a higher fraction of emitters near the 0 and 1 polarization ratios, while the histogram from 3D emitters would present a uniform ratio of 0.5. Instead, the polarization ratio histogram of our dot-in-plate NCs is consistent with 2D degenerated dipole emission.

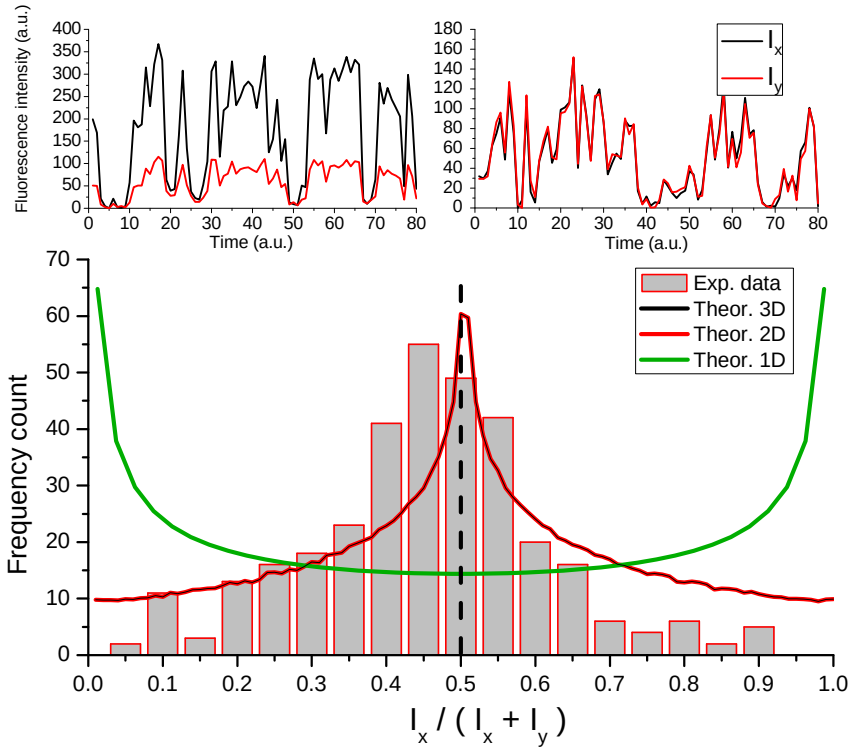

Figure S19: Upper panels, traces of single NC emission, the intensity was recorded every 200 ms. Lower panel, histogram of $\frac{I_x}{(I_x+I_y)}$, along with theoretical predictions for 1D, 2D and 3D (isotropic) degenerated dipole emission.

Differences between the theoretical polarization diagram of a 2D emitter and the experimental data in figure S19 mainly consist in a broadening of the histogram, which may be attributed to noise.

G. Emission diagram of CdSe/CdS NCs deposited on a glass coverslip

Spherical zinc blende CdSe/CdS[13] or dot-in-plates (sample P8) CdSe/CdS nanocrystals were diluted in hexane and a drop of this solution was dried on a glass coverslip. A drop of immersion oil was then deposited on top of the NCs to provide a near homogeneous refractive index environment to the NCs and reduce effects from interfaces. These NCs were observed on a fluorescence microscope (Olympus IX-71) equipped with a 100x, 1.4 NA oil immersion objective, using a 450 ± 25 nm unpolarized excitation. The NC dilution was chosen so that individual nanocrystals could be individually resolved (density << 1 μm^{-2}). At the exit port of the microscope, the image of the objective aperture is focalized at infinity. To image the

radiation diagram of these emitters, a CCD camera was thus placed at the focal plane of a 40 mm lens at the exit of the microscope. Radial profiles of the radiation diagrams obtained in the Fourier plane for spherical and dot-in-plates NCs, $R_S(k_x)$ and $R_P(k_x)$ were measured. To correct from the angular dependence of the collection efficiency of the objective, we calculate the ratio of the two profiles, $R_S(k_x)/ R_P(k_x)$.

We then compare this experimental ratio to theoretical predictions. We assume an isotropic radiation diagram for spherical NCs. The displacement along the x axis in the Fourier plane, k_x, is related to the angle between the optical axis, perpendicular to the substrate, and the emission propagation direction, by $k_x = k \sin(\theta_x)$. The intensity profile in the Fourier plane is then expressed as:

$$R_S(k_x) \propto 1/\cos(\theta_x)$$

For dot-in-plates deposited flat on the coverslip, with the c axis perpendicular to the substrate plane, and dipole emission in the (a,b) plane, the radiation diagram is

$$R_P(k_x) \propto (\cos^2(\theta_x) + \frac{1}{2}\sin^2(\theta_x))/\cos(\theta_x)$$

We then obtain

$$R_S(k_x)/R_P(k_x) \propto \cos^2(\theta_x) + \tfrac{1}{2}\sin^2(\theta_x).$$

Figure S20 shows the experimental and theoretical intensity ratio R_P/R_S as a function of the position on the x-axis of the Fourier plane. The good correlation between the two curves indicates that all dot-in-plates nanocrystals indeed deposit flat on the grid, and that they show the expected anisotropic radiation diagram.

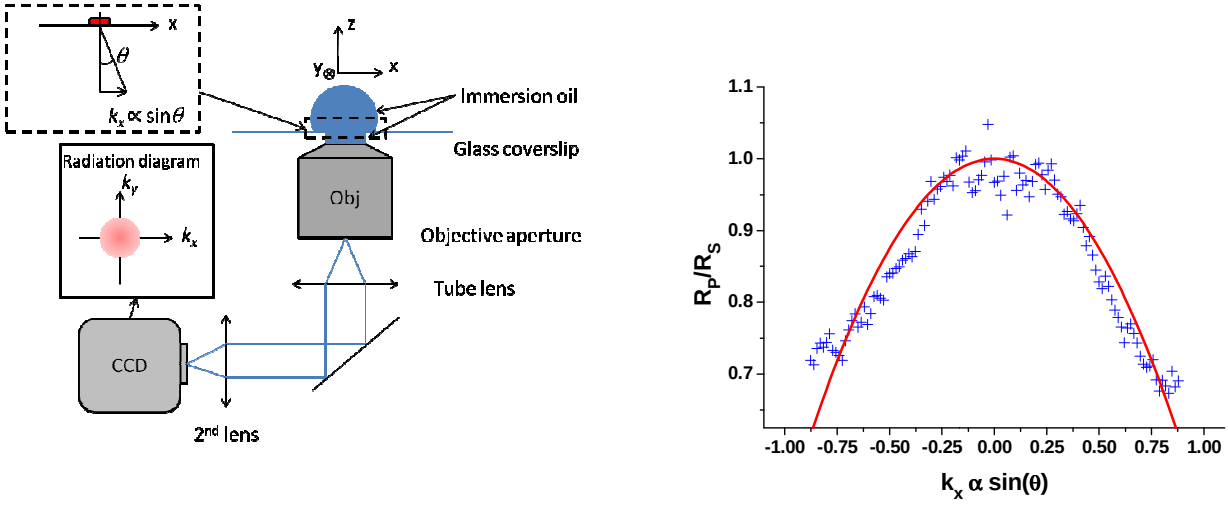

Figure S20: Left: Schematics of the set-up to image the radiation diagram of the NCs deposited on a glass coverslip. Right: Experimental (blue crosses) and theoretical (red line) intensity ratio R_P/R_S as a function of the position on the x-axis of the Fourier plane.

SI References:

1. Leatherdale, C. A.; Woo, W. K.; Mikulec, F. V.; Bawendi, M. G. On the Absorption Cross Section of Cdse Nanocrystal Quantum Dots. *J. Phys. Chem. B* **2002,** *106*, 7619-7622.
2. Yu, W. W.; Qu, L. H.; Guo, W. Z.; Peng, X. G. Experimental Determination of the Extinction Coefficient of Cdte, Cdse, and Cds Nanocrystals. *Chem. Mat.* **2003,** *15*, 2854-2860.
3. Hytch, M. J.; Snoeck, E.; Kilaas, R. Quantitative Measurement of Displacement and Strain Fields from Hrem Micrographs. *Ultramicroscopy* **1998,** *74*, 131-146.
4. Taraci, J. L.; Hytch, M. J.; Clement, T.; Peralta, P.; McCartney, M. R.; Drucker, J.; Picraux, S. T. Strain Mapping in Nanowires. *Nanotechnology* **2005,** *16*, 2365-2371.
5. Efros, A. L.; Rosen, M.; Kuno, M.; Nirmal, M.; Norris, D. J.; Bawendi, M. Band-Edge Exciton in Quantum Dots of Semiconductors with a Degenerate Valence Band: Dark and Bright Exciton States. *Phys. Rev. B* **1996,** *54*, 4843-4856.
6. Brovelli, S.; Schaller, R. D.; Crooker, S. A.; Garcia-Santamaria, F.; Chen, Y.; Viswanatha, R.; Hollingsworth, J. A.; Htoon, H.; Klimov, V. I. Nano-Engineered Electron-Hole Exchange Interaction Controls Exciton Dynamics in Core-Shell Semiconductor Nanocrystals. *Nat. Commun.* **2011,** *2*.
7. Efros, A. L., Fine Structure and Polarization Properties of Band-Edge Excitons in Semiconductor Nanocrystals. In *Nanocrystal Quantum Dots*, Klimov, V. I., Ed. CRC Press: 2010.
8. Love, A. E. H. The Mathematical Theory of Elasticity. 4th ed.; Dover: 1944.
9. Chuang, S. L.; Chang, C. S. K Center Dot P Method for Strained Wurtzite Semiconductors. *Phys. Rev. B* **1996,** *54*, 2491-2504.
10. Park, S. H.; Cho, Y. H. Strain and Piezoelectric Potential Effects on Optical Properties in Cdse/Cds Core/Shell Quantum Dots. *J. Appl. Phys.* **2011,** *109*.
11. Lakowicz, J. R. Principles of Fluorescence Spectroscopy. 3rd ed.; Springer: New York, 2006.

12. Landau, L.; Lifchitz, E.; Pitaevskii, L. Electrodynamique Des Milieux Continus. 2nd ed.; Mir: 1990.
13. Mahler, B.; Lequeux, N.; Dubertret, B. Ligand-Controlled Polytypism of Thick-Shell Cdse/Cds Nanocrystals. *J. Am. Chem. Soc.* **2010,** *132,* 953-959.